Joint Use of Far-Infrared and Mid-Infrared Observation for Sounding Retrievals: Learning from the Past for Upcoming Far-Infrared Missions

Yan Xie[1*], Xianglei Huang[1], Xiuhong Chen[1], Tristan S. L'Ecuyer[2], Brian J. Drouin[3]

[1]Department of Climate and Space Sciences and Engineering, University of Michigan, Ann Arbor, Michigan.

[2]Department of Atmospheric and Oceanic Sciences, University of Wisconsin-Madison, Madison, WI.

[3]Jet Propulsion Laboratory, California Institute of Technology, Pasadena, CA.

* Corresponding author: Yan Xie, Department of Climate and Space Sciences and Engineering, University of Michigan, Ann Arbor, Michigan 48109-2143, United States.

yanxieyx@umich.edu, +1-734-263-9631.

This is the author manuscript accepted for publication and has undergone full peer review but has not been through the copyediting, typesetting, pagination and proofreading process, which may lead to differences between this version and the Version of Record. Please cite this article as doi: 10.1029/2022EA002684.

Key Points:

- Atmospheric profiles and surface properties are simultaneously retrieved from satellite observations made 50 years ago.
- Compared to reanalysis data, the retrieval estimates produce radiances which are more consistent with the observations.
- Retrievals of humidity and temperature profiles in the lower troposphere can be considerably affected by the surface spectral emissivity.

Abstract

Atmosphere and surface properties are routinely retrieved from satellite measurements and extensively used in weather forecast and climate analysis. Satellite missions dedicated to fill the gap of far-infrared (far-IR) observations are scheduled to be launched this decade. To explore mid-infrared (mid-IR) and far-IR joint retrievals for the future far-IR satellite missions, this study uses an optimal-estimation-based method to retrieve atmospheric specific humidity and temperature profiles, surface skin temperature, and surface spectral emissivity from the Infrared Interferometer Sounder-D (IRIS-D) measurements in 1970, the only existing spaceborne far-IR spectral observations with global coverage. Based on a set of criteria, two cases in the Arctic, which are most likely under clear-sky conditions, are chosen for the retrieval experiments. Information content analysis suggests that the retrieved surface skin temperature and the mid-IR surface spectral emissivity are highly sensitive to the true values while the retrieval estimates of far-IR surface emissivity are subject to the variation of water vapor abundance. Results show that radiances based on the retrieved state variables are more consistent with the IRIS-D observations compared to those based on the reanalysis data. Retrieval estimates of the state variables along with retrieval uncertainties generally fall within reasonable ranges. The relative uncertainties of retrieved state variables decrease compared to the *a priori* relative uncertainties. In addition, the necessity to retrieve surface emissivity is corroborated by a parallel retrieval experiment assuming a blackbody surface emissivity that has revealed significant distortions of retrieved specific humidity and temperature profiles in the Arctic lower troposphere.

1. Introduction

Atmosphere and surface properties including humidity and temperature profiles, surface temperatures, and surface spectral emissivity are routinely retrieved from satellite measurements and are widely used for operational weather forecast and climate analysis. Accurate retrievals of atmospheric humidity and temperature profiles from radiances at the top-of-atmosphere (TOA) require information of the surface spectral emissivity, which plays a key role not only in the radiation budget but also atmospheric sounding. It has been demonstrated that simultaneous retrievals of atmospheric profiles and surface skin temperature with the surface spectral emissivity can substantially improve their retrieval accuracy (Plokhenko & Menzel, 2000; Ma et al., 2000; Li et al., 2007). While most retrieval studies investigate surface emissivity only in the mid-infrared (mid-IR, >667 cm^{-1}), it has been recently recognized that far-IR (≤ 667 cm^{-1}) surface emissivity have a non-negligible influence on the polar climate. Chen et al. (2014) showed that distinct bias existed in the radiation budget due to the blackbody surface assumption (i.e., $\varepsilon = 1$). Feldman et al. (2014) demonstrated the sensitivity of polar climatology projections to the specifications of surface spectral emissivity in the far-IR. A global surface emissivity dataset covering both mid-IR and far-IR (Huang et al., 2016) was implemented in the NCAR Community Earth System Model 1.1.1 and revealed differences with statistical significance in the simulations of polar climatology at the surface (Huang et al., 2018).

Despite the significance of far-IR surface emissivity for atmospheric sounding and climate projections, retrievals of surface emissivity in the far-IR are more complicated compared to those in the mid-IR. First, surface emissivity retrievals in the far-IR are subject to the strong

water vapor absorption. Mid-IR window channels can stay nearly transparent (clear-sky transmittances > 0.8) even for extremely humid scenarios (Xie et al., 2022a). However, the far-IR spectrum will become almost opaque with the clear-sky transmittances less than 0.05 when the total column water vapor (TCWV) exceeds 1 cm as indicated by Feldman et al. (2014). This implies that retrieval of far-IR surface emissivity from space-borne observations is only practical when the TCWV is small enough, such as over the polar or high-elevation regions. Second, knowledge of far-IR surface emissivity retrievals has been insufficient due to gap in the far-IR observations. Ever since the Infrared Interferometer Sounder-D (IRIS-D) was launched onboard the *Nimbus IV* (Hanel et al., 1971), no other satellite observations covering the far-IR have been operated for half a century. During its 10-month operation (April 1970 to January 1971), the IRIS-D measured nadir-view radiance spectra from 400 to 1600 cm^{-1} at a footprint of approximately 94 km in diameter (Hanel et al., 1971). Besides that, there are also some field campaigns launched recently to monitor the far-IR surface emissivity using aircraft observations over a portion of the Greenland Plateau (Bellisario et al., 2017; Murray et al., 2020).

In an effort to fill the gap of far-IR observations, two future satellite missions are selected and scheduled to be launched in this decade: PREFIRE (Polar Radiant Energy in the Far-InfraRed Experiment; L'Ecuyer et al., 2021) by NASA and FORUM by ESA (Far-infrared Outgoing Radiation Understanding and Monitoring; Palchetti et al., 2020) will open up a new era for far-IR surface emissivity retrievals in polar regions. Previous work has shown promising results with surface spectral emissivity retrieved in mid-IR and far-IR from simulated PREFIRE measurements in the Arctic (Xie et al., 2022a) and simulated FORUM observations

at different latitudes including polar regions (Ridolfi et al., 2020; Sgheri et al., 2022). It is therefore necessary and interesting to carry out a retrieval effort with real far-IR satellite observations. The IRIS-D observations, even made half a century ago, still remain as the only existing space-borne, spectrally resolved measurements covering the far-IR spectrum. It thus provides an opportunity to investigate the feasibility of simultaneously retrieving atmospheric humidity and temperature profiles, surface temperatures, and mid- and far-IR surface spectral emissivity in the Arctic.

A large variety of algorithms have been implemented to retrieve atmospheric profiles and surface parameters. These retrieval techniques generally fall into two categories: statistical methods or physical methods (Maahn et al., 2020). Statistical methods utilize empirical relationships and assumptions to solve the inverse problems (Maahn et al., 2020). However, when the empirical relationships cannot hold true anymore, the retrieval results of these statistical methods become problematic (Becker & Li, 1990). Physical methods, however, depend less on empirical assumptions and approach the solutions through iterative steps. For example, the optimal estimation (OE) method seeks the solution iteratively by minimizing the mismatch between the simulations by forward radiative transfer model and the observations. The OE method is based on the Bayesian framework, combining the *a priori* knowledge and observations to generate retrieval results with inherent uncertainty estimates (Rodgers, 2000). This method has a widespread use in retrievals of atmospheric profiles and surface properties (L'Ecuyer and Stephens, 2002; Li et al., 2000; Liu et al., 2009; Scarlat et al., 2017; Turner & Löhnert, 2014; Wood and L'Ecuyer, 2021), also in the retrievals of both atmospheric profiles and surface properties in either a sequential (Susskind et al., 2003) or simultaneous (Ma et al.,

2000; Li et al., 2007) way. These successful applications of the OE method thus encourage us to apply it to the simultaneous retrieval of atmospheric profiles and surface properties.

This study seeks to implement the OE method to simultaneously retrieve atmospheric specific humidity and temperature profiles, surface temperatures, and surface spectral emissivity in mid-IR and far-IR using the IRIS-D observations in the Arctic. Section 2 introduces the data and the forward radiative transfer model used in the study. Details of the OE-based retrieval framework are described in Section 3. Section 4 presents the information content analysis and retrieval experiment results, followed by conclusions and discussions in Section 5.

2. Data and Forward Modeling

2.1 IRIS-D spectral radiances

The IRIS-D onboard the *Nimbus IV* is a single detector Michelson interferometer (Hanel et al., 1971). The IRIS-D instrument measured outgoing spectral radiances covering 400 to 1600 cm^{-1} at a nominal spectral resolution of 2.8 cm^{-1} in nadir view from April 1970 to January 1971. IRIS-D operated in a near-polar orbit at the height of 1100 km with a footprint of approximately 94 km in diameter. Over the ten-month operation period, IRIS-D has collected around 700,000 calibrated spectra in total. IRIS-D was an instrument well ahead of the time. It was the prototype of two IRIS instruments aboard Voyager1 and Voyager2 that recorded detailed infrared spectra of outer planets during their flybys. Decades after its operation ended, its measurements were still used to infer climate change signals (Harries et al., 2001), to test climate models (Haskins et al., 1999; Huang et al., 2002), and to evaluate the clear-sky flux biases in the climate model (Huang et al., 2006).

The noise-equivalent spectral radiances (NeSRs) of IRIS-D are mostly between 0.5 and 1.0 $\mathrm{mW \cdot m^{-2} \cdot sr^{-1} / cm^{-1}}$, but tend to be higher at both the ends of the spectral range. The estimates of IRIS-D NeSRs shown in Hanel et al. (1972) are used in our study to characterize noise level on each channel. To be more specific, measurement noises on each IRIS-D channel are assumed to follow the Gaussian distribution with zero mean and the corresponding NeSR as the standard deviation.

Due to the small signal-to-noise ratio at frequencies higher than 1400 $\mathrm{cm^{-1}}$ (Haskins et al., 1997), only the channels from 400 to 1400 $\mathrm{cm^{-1}}$ are considered as done in previous studies using the IRIS-D data (Huang et al., 2002; Huang et al., 2006). Besides that, channels significantly affected by absorption of greenhouse gases other than H_2O and CO_2, i.e., O_3, CO, N_2O and CH_4, are excluded from the retrieval as shown by the gray shades in Figure 1a. The atmospheric CO_2 concentration data used in the study are from the monthly mean observations by NOAA Global Monitoring Laboratory (Tans & Keeling, 2022). In total, 406 out of 862 IRIS-D channels are selected for the retrieval.

2.2 ERA5 back extension reanalysis data

The ERA5 reanalysis is generated on the basis of the Integrated Forecasting System (IFS) Cy41r2 with a 4-D variational data assimilation scheme by the European Centre for Medium-Range Weather Forecasts (ECMWF) (Hersbach et al., 2020). Recently, Bell et al. (2021) developed a back-extended segment of ERA5 reanalysis covering the period from January 1950 to December 1978, which incorporated supplementary conventional observations and early satellite data. This ERA5 extension provides hourly estimates of essential atmospheric and surface variables over the globe with a 0.25º-by-0.25º spatial resolution and covers 37

pressure levels from the surface up to 1hPa in the vertical direction. Compared to other ECMWF reanalysis extended back to the 1950s, the ERA5 extension provides higher spatial and temporal resolution. The fidelity of the ERA5 extension has been demonstrated by showing an ability to accurately depict well-known synoptic events in 1952 and 1953 (Bell et al., 2021). Also, since the number of assimilated observations increases by over 10 times from 1950 to 1978, the reanalysis quality is presumed to improve steadily in the 1970s.

2.3 Surface spectral emissivity data set

Huang et al. (2016) developed a surface spectral emissivity dataset which covers the whole longwave spectrum with a horizontal resolution of 0.5°-by-0.5° all over the globe. This surface emissivity dataset includes various surface types such as water, ice, snow (fine, medium and coarse), conifer, grass, tundra, and desert (Huang et al., 2016). The mid-IR surface emissivity in this dataset were validated against retrievals from IASI observations (Huang et al., 2016; Zhou et al., 2011). Since there are no far-IR observations applicable yet to validate this global dataset, the far-IR surface emissivity in this dataset is derived from either first-principle calculations or extrapolation depending on the surface type. More information about this surface emissivity dataset is available in Huang et al. (2016). Due to the lack of any observationally based far-IR surface emissivity dataset, our study uses this dataset to construct the *a priori* mean and covariance for the surface spectral emissivity.

2.4 Forward radiative transfer model PCRTM

The forward radiative transfer model plays a key role in the retrieval scheme by mapping the retrieval estimates into the measurement space at each iteration step. Liu et al. (2006) developed the Principal Component-based Radiative Transfer Model (PCRTM) V3.4 which

utilizes the inter-channel correlation to decrease the computational cost. It has been demonstrated that the root-mean-square error (RMSE) of brightness temperature between the PCRTM calculations and benchmark calculations is smaller than 0.4K (Liu et al., 2006). In addition, it has been showed by Chen et al. (2013) that the RMSE of brightness temperature between the PCRTM V2.1 and the LBLRTM (Line-By-Line Radiative Transfer Model) 12.0 (Clough et al., 2005) can be 0.67K under clear-sky conditions, while the PCRTM requires approximately only 0.02% of the computation time that LBLRTM takes. A PCRTM-based simulator has been developed by Chen et al. (2013) and successfully applied in multiple studies (Huang et al., 2014; Bantges et al., 2016; Chen et al., 2018; Xie et al, 2022a). It is applied in our study as the forward model to calculate spectral radiances and Jacobians in clear-sky conditions.

3. Methodology

3.1 Selection of clear-sky cases

This study is focused on retrievals in clear-sky conditions only. The ERA5 hourly reanalysis data has been interpolated to the time and location of each IRIS-D measurement. A multiple-step approach is used to identify clear-sky spectra. First, spectra observed over the Arctic Ocean are chosen for less ambiguity in classification of surface types using retrieved surface spectral emissivity. Surface emissivity spectra of various kinds of surface types, such as water, ice, snow, tundra, grass, conifer, are all used in constructing the *a priori* constraints in the retrieval procedure. Then a tri-spectral method developed by Ackerman et al. (1990) is used to determine whether the input radiance spectrum is under clear- or cloudy-sky condition. Based on the different spectral absorption features of water vapor, liquid and ice clouds at 8 μm, 11 μm and

12 μm bands, if the brightness temperatures difference is negative between 8 μm and 11 μm bands and positive between 11 μm and 12 μm bands, the spectra is deemed to be under clear-sky condition (Ackerman et al., 1990). This method has been applied to IRIS-D measurements before (Huang et al., 2006). Thirdly, for the IRIS-D spectra classified as clear-sky in the previous step, the maximum brightness temperatures over the mid-IR window region (900-970 cm^{-1} and 1090-1200 cm^{-1}) are then compared against the corresponding surface temperatures as derived from the ERA5 reanalysis. The transmittances of mid-IR window channels can be 0.94 or higher under the clear-sky conditions, which implies the maximum mid-IR brightness temperatures should be close to surface temperatures if the footprint was indeed clear-sky. Finally, the synoptic weather patterns for each spectrum that pass the previous three steps are examined. The footprint of IRIS-D is around 94 km in diameter, several factors larger than those of current hyperspectral sounders (which is ~10-15km in diameter), which means clear Arctic footprints at this large field of view are rare to find. Given this fact, the synoptic analysis is especially useful to the selection of clear-sky cases. If the synoptic weather patterns over the identified satellite footprints are patterns favoring clear sky more than cloudy sky, it can further increase our confidence about the clear-sky detection.

Two qualified cases are chosen according to the abovementioned requirements, one in April and the other in July 1970, referred to as Case 1 and Case 2 respectively. Geolocation, time, and surface pressure of the two selected cases are listed in Table 1. Figure 1a and Figure 2a show the respective spectra in brightness temperature and the surface temperatures. For both cases, the absolute difference between the maximum brightness temperature of the spectra over mid-IR window region and surface temperature is less than 3K. The synoptic weather fields

for the two cases are summarized in Figure 1b/1c and 2b/2c, respectively. The ground footprints of both cases (black star on the plot) are under deep high-pressure weather systems. Such weather systems are featured with upper-level convergency and low-level divergency, indeed favoring clear sky rather than cloud formation.

3.2 Optimal estimation method

The retrieval algorithm used here largely follows the optimal estimation (OE) method described in Rodgers (2000) and Xie et al. (2022a). According to the Bayes' theorem,

$$\mathrm{P}(\mathbf{x}|\mathbf{y}) = \frac{\mathrm{P}(\mathbf{y}|\mathbf{x}) \cdot \mathrm{P}(\mathbf{x})}{\mathrm{P}(\mathbf{y})} \tag{1}$$

where $\mathbf{y}$ denotes the radiances observed at TOA and $\mathbf{x}$ denotes the state vector. $\mathrm{P}(\mathbf{x})$ represents the *a priori* probability distribution of the state variable $\mathbf{x}$. In this study $\mathbf{x}$ = ($\mathbf{q}$, $\mathbf{T}$, T_S, $\boldsymbol{\varepsilon_\nu}$), with $\mathbf{q}$ and $\mathbf{T}$ vectors refer to the specific humidity and air temperature profiles, T_S the surface skin temperature, and $\boldsymbol{\varepsilon_\nu}$ the surface spectral emissivity. $\mathrm{P}(\mathbf{x}|\mathbf{y})$ represents the *posteriori* probability, a conditional probability distribution of $\mathbf{x}$ given the observation $\mathbf{y}$. $\mathrm{P}(\mathbf{y})$ serves a normalization term and can be seen as a constant. Based on the assumption that the *a priori* $\mathrm{P}(\mathbf{x})$ and the likelihood $\mathrm{P}(\mathbf{y}|\mathbf{x})$ both follow Gaussian distributions, the derived $\mathrm{P}(\mathbf{x}|\mathbf{y})$ is therefore also a Gaussian-distributed probability. The OE method solves the retrieval problem by iteratively approaching the optimal estimate $\hat{\mathbf{x}}$ that maximizes $\mathrm{P}(\mathbf{x}|\mathbf{y})$. The *posteriori* covariance matrix $\hat{\mathbf{S}}$ evaluates the retrieval uncertainty. $\hat{\mathbf{x}}$ can be estimated iteratively using the Gauss-Newton method in moderately linear cases (Rodgers 2000). Retrieval estimates of $\hat{\mathbf{x}}$ at the (i+1)-th iteration step, $\mathbf{x}_{i+1}$, can be written as

$$\mathbf{x}_{i+1} = \mathbf{x}_a + \left(\gamma \mathbf{S}_a{}^{-1} + \mathbf{K}_i{}^T \mathbf{S}_\epsilon{}^{-1} \mathbf{K}_i\right)^{-1} \mathbf{K}_i{}^T \mathbf{S}_\epsilon{}^{-1} [\mathbf{y} - \mathrm{F}(\mathbf{x}_i) + \mathbf{K}_i(\mathbf{x}_i - \mathbf{x}_a)] \tag{2}$$

The corresponding retrieval uncertainty $\hat{\mathbf{S}}$ at the i-th iteration can be expressed as

$$\mathbf{S}_i = \left(\gamma \mathbf{S}_a{}^{-1} + \mathbf{K}_i{}^T \mathbf{S}_\epsilon{}^{-1} \mathbf{K}_i\right)^{-1} \left(\gamma^2 \mathbf{S}_a{}^{-1} + \mathbf{K}_i{}^T \mathbf{S}_\epsilon{}^{-1} \mathbf{K}_i\right) \left(\gamma \mathbf{S}_a{}^{-1} + \mathbf{K}_i{}^T \mathbf{S}_\epsilon{}^{-1} \mathbf{K}_i\right)^{-1} \quad (3)$$

$\mathbf{x}_a$ and $\mathbf{S}_a$ are the *a priori* mean and covariance matrix of $\mathbf{x}$, containing information of state variables known before the measurements take place. The noise covariance $\mathbf{S}_\epsilon$, which is a diagonal matrix composed of the squared IRIS-D NeSRs, denotes the uncertainty contributed by measurement noise ϵ. The Jacobian matrix $\mathbf{K} = \partial \mathrm{F}(\mathbf{x})/\partial \mathbf{x}$ is computed as the derivative of TOA radiances with respect to the state variables, which can be generated by the forward model PCRTM. The tuning parameter γ in Eqs.2-3 is introduced to modify the weightings of *a priori* constraints and observation information (Carissimo et al., 2005; Zhou et al., 2007; Turner and Löhnert, 2014). A series of γ values starting from 1000 then gradually decreasing to 1 are applied to the formulas following the previous study by Turner and Löhnert (2014), which is meant to increase the weighting of observations step by step to stabilize the retrieval process against measurement noises. The convergence criterion (Eq. 4) indicates that the difference in retrieval estimates between two successive steps when converged should be negligible compared to the retrieval uncertainty.

$$(\mathbf{x}_i - \mathbf{x}_{i+1})^T \mathbf{S}_i{}^{-1} (\mathbf{x}_i - \mathbf{x}_{i+1}) < \frac{length(\mathbf{x})}{10} \quad (4)$$

The iteration will stop when the tunning parameter equals 1 and the convergence criterion is satisfied.

3.3 Transformation of state variables

3.3.1 Specific humidity

Since the sensitivity of infrared radiances to water vapor in the stratosphere is relatively low (Susskind et al., 2003; Davis et al., 2017), retrievals of water vapor profile using infrared satellite measurements usually focus on the troposphere. In this study, only tropospheric

specific humidity profiles below 200hPa are retrieved, and those above 200hPa are prescribed with the corresponding seasonal mean profiles as in the ERA5 back-extension reanalysis.

Previous studies have shown that the logarithmically transformed specific humidity can fit the Gaussian distribution better than the original humidity profiles (Masiello et al., 2018; Maahn et al. 2020). Figure 3a shows the probability distribution of ERA5 hourly specific humidity at 500hPa in March, April, and May 1970 over the Arctic. And Figure 3c presents a quantile-quantile plot (Q-Q plot) comparing the quantiles of 100 samples randomly drawn from this specific humidity distribution to the quantiles of a standard normal distribution. If the samples followed a Gaussian distribution, the data points would fall along a straight line in the Q-Q plot. As shown in Figure 3c, although the samples fit fairly with the standard normal distribution between the first and third quantiles, the consistency no longer holds true beyond this range. On the other hand, Figure 3b and 3d provide a glance at the distribution and Q-Q plot of logarithmically transformed specific humidity. The probability density function (PDF) of logarithmic specific humidity now resembles a Gaussian curve much more than the PDF of original specific humidity does (Figure 3b). Figure 3d also indicates that compared to the specific humidity, its logarithmic transformation fits the Gaussian distribution more closely. Therefore, the logarithm of specific humidity profiles, log(q), is treated as a state variable to retrieve specific humidity in the OE algorithm. The Jacobians of logarithmic specific humidity $\mathbf{K}_{\log(q)}$ can be calculated using the chain rule

$$\mathbf{K}_{\log(q)} = \frac{\partial \mathbf{F}(\mathbf{x})}{\partial \log(q)} = q \frac{\partial \mathbf{F}(\mathbf{x})}{\partial q} = q\mathbf{K}_q \quad (5)$$

where $\mathbf{K}_q$ can be conveniently calculated by the PCRTM.

3.3.2 Surface spectral emissivity

It has been demonstrated that the retrieval uncertainties of mid-IR surface spectral emissivity using satellite observations can vary from 0.005 to 0.04 with a median value around 0.02, depending on multiple factors such as wavenumbers of surface emissivity, noise levels of the measurements, meteorological conditions, surface types, retrieval algorithms, and validation methodology (Faysash and Smith, 2000; Gillespie et al., 1998; Li et al., 2007; Masiello et al., 2018; Wan 2008). Figure 4 shows that the changes of radiances due to a perturbation of 0.02 in the surface spectral emissivity are distinguishable from the IRIS-D measurement noise level. The radiances differences of Case 1 and Case 2 mostly exceed the IRIS-D NeSRs over the 755 to 970 cm^{-1} mid-IR window region. In the far-IR, radiances changes of Case 1 are comparable to the NeSRs from 495 to 556 cm^{-1} while those of Case 2 are close to zero as a result of the enhanced water vapor absorption in July.

Different from the jagged radiances spectra with spiky absorption lines, the surface emissivity spectra are typically smoother and can be well characterized at a spectral interval of 10 cm^{-1} (Borel, 1998; Huang et al., 2016). Thus, surface spectral emissivities are retrieved on the channels at an interval of 10 cm^{-1} in this study, which are denoted by the black horizontal lines in Figure 4. In total, there are 58 channels for surface emissivity retrievals, with 37 mid-IR channels and 21 far-IR channels.

Surface emissivity is physically bounded between 0 to 1. However, the OE retrieval framework does not set hard boundary conditions for the surface spectral emissivity, therefore it is possible for the retrieval algorithm to converge on an unrealistic surface spectral emissivity exceeding unity. To avoid such an issue, the surface spectral emissivity ε_ν (ν refers to the wavenumber) is projected to an unbounded range through the logit transformation (Masiello et

al., 2018).

$$Z_\nu = \mathrm{logit}(\varepsilon_\nu) = \log\left(\frac{\varepsilon_\nu}{1-\varepsilon_\nu}\right) \quad (6)$$

In this way, the logit of surface emissivity is updated iteratively in the retrievals. And when transformed back, the optimal estimates of surface spectral emissivity are assured to be within the range [0,1]. The formula of Jacobians for the logit-transformed surface emissivity, $\mathbf{K}_{z_\nu}$, can be written as

$$\mathbf{K}_{z_\nu} = \frac{\partial \mathbf{F}(\mathbf{x})}{\partial\, \mathrm{logit}(\varepsilon_\nu)} = \frac{\partial \mathbf{F}(\mathbf{x})}{\partial \varepsilon_\nu}\varepsilon_\nu(1-\varepsilon_\nu) \quad (7)$$

3.4 Construction of *a priori* constraints

In Eqs.1-4, $\mathbf{S}_\epsilon$ is a diagonal matrix determined by the IRIS-D instrument noise level. $\mathbf{K}$ are obtained from the PCRTM output. While the *a priori* constraints $\mathbf{x}_a$ and $\mathbf{S}_a$ are constructed more subjectively compared to $\mathbf{K}$ and $\mathbf{S}_\epsilon$.

A priori information of the state variables is available from a large variety of sources including records of meteorological and climatological fields, laboratory experiments, and empirical knowledge. There are significant seasonal variations in the temperature and humidity profiles in the Arctic. Therefore, the *a priori* constraints for humidity and temperature profiles in this study are seasonal-dependent. The *a priori* mean $\mathbf{x}_a$ for logarithmic specific humidity profiles, air temperature profiles and surface temperatures are calculated as the seasonal mean based on the ERA5 hourly reanalysis data in the Arctic. And the corresponding *a priori* covariance $\mathbf{S}_a$ is modified based on the original covariance by halving the off-diagonal values in order to weaken the effect of intercorrelation between different state variables. On the other hand, the seasonal changes of surface spectral emissivity are within a smaller range. For surface spectral emissivity, the *a priori* mean $\mathbf{x}_a$ is calculated as the annual mean averaged over the

Arctic using the global surface emissivity dataset (Huang et al., 2016) mentioned above. The *a priori* covariance is constructed from the same surface emissivity dataset. Surface spectral emissivity in nadir view is averaged on each IRIS-D channel, then the covariance matrix is calculated based on the surface emissivity spectra in the Arctic at the IRIS-D spectral resolution. Note that there are no far-IR observations available yet to confirm the accuracy of the global surface emissivity dataset (Huang et al., 2016). Therefore, it would be problematic to treat the calculated covariance from the emissivity dataset as the *a priori* covariance $\mathbf{S}_a$: the directly calculated covariance may underestimate the realistic variations of surface emissivity spectra and result in a too tight *a priori* constraint to allow information from observations to be retrieved. To cope with this, further adjustments are made to construct a relatively loose *a priori* covariance $\mathbf{S}_a$. First of all, *a priori* spread of surface spectral emissivity is doubled based on the calculated values to allow a larger variation range for the retrieval estimates. In addition, the correlation coefficients among surface emissivity on different channels are decreased by half to reduce the influence of *a priori* inter-channel correlations on the surface emissivity retrievals.

4. Results

4.1 Evaluation of information content

Information content estimates the amount of information arising from the true state variables which are retrievable from the noisy measurements. The averaging kernel (Backus et al., 1970) and the degree of freedom (DoF) for signal (Rodgers, 2000) are two metrics which are used here to quantitatively evaluate the information content. The averaging kernel $\mathbf{A}$ characterizes the change of retrieval estimates in response to variations in the true state

variables,

$$\mathbf{A} = \frac{\partial \hat{\mathbf{x}}}{\partial \mathbf{x}} = \mathbf{S}_a \mathbf{K}^T (\mathbf{K}\mathbf{S}_a \mathbf{K}^T + \mathbf{S}_\epsilon)^{-1} \mathbf{K} \quad (8)$$

The DoF for signals d_s is defined as the number of independent pieces of information contributed by the true state variables which can be retrieved (Rodgers 2000) considering the *a priori* covariance, measurement noise, and sensitivity of measurements to state variables, and equals the trace of the averaging kernel $\mathbf{A}$.

$$d_s = \sum \mathrm{diag}(\mathbf{A}) \quad (9)$$

Averaging kernels of some state variables in Case 1 are shown in Figure 5. The averaging kernels of logarithmic specific humidity (Figure 5a) and air temperature (Figure 5b) generally have their maximum at the corresponding pressure level and relatively low values everywhere else, which indicates the retrieval estimates are most sensitive to its own true value and can also be modestly affected by other state variables. It is noticeable that the averaging kernel of logarithmic specific humidity on 400hPa has its maximum near 550hPa instead of 400hPa. This implies the retrieved specific humidities in the upper troposphere tend to be more sensitive to water vapor changes in the middle troposphere, which is likely owing to the fact that most water vapor channels used in our study are responsive to changes in the mid-troposphere instead of upper troposphere (most upper-tropospheric water vapor channels are between 1400-1600 cm^{-1}, which are not used due to the large NeSR). The averaging kernels of surface properties are superior to those of atmospheric profiles, with the narrow peaks close to 1 for surface skin temperature (Figure 5c) and surface emissivity on several channels in mid-IR and far-IR (Figure 5d). Table 2 lists the DoF for signals of all the state variables including logarithmic specific humidity profile on 23 ERA5 pressure levels from 200hPa to 1000hPa, air

temperature profile on 37 ERA5 pressure levels from 1hPa to 1000hPa, surface skin temperature, and logit-transformed surface spectral emissivity from 400 to 1400 cm^{-1} with 37 out of 58 channels in the mid-IR and the rest 21 channels in the far-IR. The d_s values of air temperature profile, surface skin temperature, and mid-IR surface spectral emissivity almost hold constant despite the different meteorological conditions of the two cases. While the d_s values of specific humidity profile and far-IR surface emissivity are subject to seasonal variations to different extents. The d_s value of far-IR surface emissivity for Case 2 in July is less than one-thousandth of that for Case 1 in January as shown in Table 2, which is consistent with what is shown in Figure 4. This decrease of d_s is mainly due to the increased water vapor abundance in summer and thus enhanced atmospheric absorption over the far-IR.

4.2 Retrieval experiment with IRIS-D observations

The OE framework is applied to the two selected cases for the retrieval of both atmospheric and surface properties. For both Case 1 and Case 2, the retrieval converged within 10 iterations. Differences between the radiances based on the retrieved state variables and the corresponding IRIS-D observations, i.e., the residual radiances, are shown in Figure 6 for both cases. The residual radiances mostly fall within the range of measurement noises denoted by the shade. For Case 1, the RMSE of residual radiances is 0.67 $mW \cdot m^{-2}sr^{-1}/cm^{-1}$ for the selected channels represented by the solid curve. The dashed curve stands for the difference between radiances based on the initial guess of state variables and the observations, of which the RMSE is 1.59 $mW \cdot m^{-2}sr^{-1}/cm^{-1}$. Similarly for Case 2, the RMSE of residual radiances are 0.90 $mW \cdot m^{-2}sr^{-1}/cm^{-1}$ and 1.42 $mW \cdot m^{-2}sr^{-1}/cm^{-1}$ for the radiance spectra based on retrieval estimates and initial guess respectively. It is noteworthy that this improved consistency

in radiance spectra from the initial step to the convergence step is not only reflected by the selected channels, but also occur over the channels not selected for the retrieval which are denoted by the dotted lines in Figure 6. This indicates the retrieved state variables indeed represent a physical projection of the IRIS-D observations into the state space, rather than overfitting the measurements on the selected channels at the sacrifice of accuracy on the rest unselected channels.

For Case 1 and Case 2, the initial guesses are based on the humidity and temperature profiles from the ERA5 reanalysis which are denoted by the blue curves in Figure 7a/7b and Figure 8a/8b, and a graybody assumption of surface spectral emissivity at 0.95. Retrieval estimates of state variables for Case 1 are shown in Figure 7. The retrieved specific humidity profile agrees with the ERA5 reanalysis profile in the upper troposphere above 500hPa (Figure 7a). Differences between the retrieved profile and ERA5 profile below 500hPa can be as large as 0.21 g/kg near 650hPa and 0.34 g/kg near 950hPa, mostly due to the vertical variations of the ERA5 specific humidity profile in the middle and lower troposphere. Figure 7b exhibits the retrieved air temperature profile from 1hPa to 1000hPa as well as the surface skin temperature. The retrieved air temperature profile is highly consistent with the ERA5 reanalysis temperature profile above 300hPa. In the troposphere, the retrieved temperatures tend to be colder than the reanalysis values with the largest discrepancy of approximately 10.4 K between 800hPa and 900hPa. The retrieval uncertainty of tropospheric temperatures, as denoted by the shade range, gradually increases from a standard deviation of 3.4 K at the tropopause to 7.5 K at 1000hPa. As a reference, the corresponding *a priori* uncertainty is 4.3 K at 300hPa and 10.5 K at 1000hPa. This decrease of uncertainty level from the *a priori* knowledge to the retrieval estimates reflects

the contribution of satellite measurements to further narrowing down the range of temperature profiles in the troposphere. The retrieved surface skin temperature at 1027.2hPa is lower than the ERA5 reanalysis value by 3.4 K, with a retrieval uncertainty of 0.3 K, which is much smaller than those of the air temperature retrievals. Figure 7c shows the retrieved surface spectral emissivity together with the spectral emissivities of pure ice and water surfaces from Huang et al. (2016). The retrieved surface spectral emissivity values are between 0.93 and 0.99 and comparable with the ranges of ice and water emissivity spectra. Note that the spectral smoothness of the retrieved surface emissivity is not similar to those of the ice and water emissivity spectra, which also makes it difficult to categorize the surface type to either one. Possible reasons for this phenomenon include the impact of measurement noises and the interplay between different state variables in the retrieval. The retrieval uncertainties of surface spectral emissivity on the channels between 400 to 450 cm^{-1}, and 600 to 700 cm^{-1} are more than twice of those in the mid-IR, which mostly reflect the *a priori* uncertainty rather than information from the measurements. This is because of the atmospheric absorption over these spectral ranges, which can also be corroborated by the relatively low Jacobian values at the corresponding wavenumbers in Figure 4. As shown in Table 3, the decrease from the *a priori* to the *posteriori* average relative uncertainty shows that the IRIS-D observations have effectively narrowed down the variation ranges of atmospheric profiles and surface properties in the retrievals. The average relative retrieval uncertainties of state variables in Case 1 are 25.7% for the logarithmic specific humidity, 2.4% for air temperature, 0.1% for surface skin temperature, 16.7% and 8.5% for the mid-IR and far-IR surface emissivity on the logit scale (Table 3), among which the average relative uncertainties of specific humidity and surface skin

temperature decrease by the largest extents.

As for Case 2, the retrieval estimates of both specific humidity and temperature profiles are consistent with the ERA5 reanalysis profiles. The retrieved specific humidity profile in July has a wider range of variation from 0.004 g/kg at 200hPa to 1 g/kg near surface (Figure 8a), almost five times larger than those of Case 1 in April. While for the air temperature profile, the retrieval uncertainty is now 6.4 K at 1000hPa and smaller by approximately 1 K compared to that in the Case 1 on every pressure level in the middle and lower troposphere (Figure 8b). The retrieved surface skin temperature at 1015.1hPa is a bit colder than the ERA5 reanalysis estimate by 2.2K, with a retrieval uncertainty of 0.4 K. The retrieval estimate of surface spectral emissivity is shown in Figure 8c. The retrieval uncertainty of surface emissivity in the far-IR can be up to 0.15, which is dominated by the *a priori* constraint instead of information from the measurements because of the water vapor absorption predominant in the far-IR during summer. This relatively large *a priori* uncertainty level is not directly calculated from the surface emissivity dataset (Huang et al., 2016) but from the logit-transformed surface spectral emissivity, and then manually doubled on the logit basis, which makes it loose enough to allow more weightings given to the measurements by the retrieval framework. Although the spectral characteristics of retrieved surface emissivity are within a reasonable range from the perspective of the retrieval algorithm, they did not provide conclusive information on the possible surface types. Since Case 1 and Case 2 differ in geolocation and season, it is expected that the retrieved surface spectral emissivity of these two cases are different from each other. As shown in Table 3, the average relative retrieval uncertainties of state variables in Case 2 are 58.3% for the logarithmic specific humidity, 1.2% for air temperature, 0.1% for surface skin

temperature, 28.8% and 9.4% for the mid-IR and far-IR surface emissivity on the logit scale.

In order to further investigate the influence of blackbody surface assumption on retrieval results, a parallel experiment is performed with all settings the same except the surface spectral emissivity values being fixed at unity (i.e., blackbody surface) Differences in the retrieval estimates of specific humidity and temperature profiles between the two setups are shown in Figure 9. According to the two cases in the Arctic, the blackbody surface assumption distorts the retrieval estimates of atmospheric humidity and temperature profiles more distinctly in the lower troposphere. The decrease in retrieved specific humidity and temperature can be as large as 0.4 g/kg and 6.5K at 1000hPa. For both cases, the retrieved surface skin temperatures based on the assumption of a blackbody surface are lower than those shown in Figure 7 and 8 by around 3K, which is an inevitable consequence of the overestimated surface emissivity values.

5. Conclusions and discussion

Retrieval products of atmospheric profiles and surface properties are widely used for weather analysis and climate research. Atmospheric sounding using satellite observations requires accurate information of surface spectral emissivity. It has been recently acknowledged that far-IR surface emissivity is important to polar climate, which motivates the selection of satellite missions dedicated to fill the gap of far-IR observations in this decade. The launch of future far-IR satellite missions will bring unprecedented opportunities for retrievals in the polar regions and would also benefit from retrieval studies using real satellite measurements. Therefore, this study seeks to simultaneously retrieve atmospheric profiles and surface properties using IRIS-D observations, an antique dataset which is also currently the only available far-IR satellite measurements, with a hope to provide a valuable reference for future

far-IR satellite missions.

Given the large footprint of IRIS-D and the frequent occurrence of clouds in the Arctic, a multiple-step clear-sky selection method is applied to filter the IRIS-D measurement. Two cases are chosen for the retrieval experiments. Information content analysis of the two cases indicate adequate information content for retrievals of surface skin temperature and surface spectral emissivity. In addition, the DoF for signals of far-IR surface emissivity decreases rapidly as the water vapor absorption becomes stronger. A retrieval framework based on the OE method has been implemented to perform simultaneous retrieval using mid- and- far-IR radiances. Specific humidity profiles and surface spectral emissivity are mathematically transformed for better retrieval performance. Both cases converge within 10 iterations.

It has been demonstrated that radiances based on the retrieved state variables are more consistent with the IRIS-D observations than those based on the reanalysis estimates. This improved consistency occurs not only at the selected IRIS-D channels for retrievals but also at the channels not used for the retrievals, which indicates the retrieved state variables indeed represent a more accurate projection of the satellite observations. Retrieved specific humidity and air temperature profiles are smoothly varying. The retrieved surface skin temperatures have a narrow variation range and differ from the ERA5 reanalysis value by around 3 K. Radiance changes in response to an uncertainty level of 0.02 in the surface spectral emissivity are distinguishable from the IRIS-D measurement noises. The retrieval estimates of surface spectral emissivity generally fall within a reasonable range with the retrieval uncertainty varying between 0.006 and 0.15. The average relative retrieval uncertainties of state variables in Case 1 (Case 2) are 25.7% (58.3%) for the logarithmic specific humidity, 2.4% (1.2%) for

air temperature, 0.1% (0.1%) for surface skin temperature, 16.7% (28.8%) and 8.5% (9.4%) for the mid-IR and far-IR logit-transformed surface emissivity. These average relative uncertainties decrease by different extents compared to the *a priori* relative uncertainties, which indicates that information from the IRIS-D measurements has helped to narrow the variation ranges of state variables in the retrievals. In addition, a parallel retrieval experiment based on the blackbody assumption for surface emissivity has revealed significant distortion of retrieved specific humidity and temperature profiles in the lower troposphere.

The sensitivity of retrieved state variables to the initial guess has also been investigated by applying a series of different initial guess values to the retrieval framework (not shown here). Our results suggest that the retrieval estimates are mostly insensitive to the variation of initial guess values. For example, in a scenario when the initial guess of specific humidity profile is increased by 395% to 405% randomly at each level, the temperature profile is increased by 19.8K to 20.2K at each level, and surface spectral emissivity is randomly perturbed between -0.01 and 0.01, changes in retrieval estimates and uncertainty level are less than 0.1%. In this study, the bias between IRIS-D observations and the forward modeling has not been quantitatively considered in the retrieval algorithm. While we are aware of the existence of such bias, to quantify the bias requires extremely accurate characterization of the atmospheric profiles at the exact geolocation and time when the radiance spectra are observed, which is usually obtained through in-situ measurements. As the IRIS-D radiances were measured half a century ago, there was no chance to accurately quantify these bias values. Ignoring such biases would inevitably affect the retrieval results to some extent, but this defect can be improved in the algorithm development for the upcoming PREFIRE and FORUM missions with carefully

planned calibration and validation field campaigns. Another thing worth noting is that by simulating radiances at a finer spectral resolution than that of IRIS-D, the DoF for signals of specific humidity profiles and surface spectral emissivity are distinctly increased. For example, if we perform the radiance simulation at 0.4 cm^{-1} spectral resolution (full width half maximum), i.e., a spectral resolution comparable to that of FORUM, the DoFs for humidity profiles, mid-IR and far-IR surface spectral emissivity in Case 1 become 2.3, 176.4 and 58.5, respectively. Given the fact that FORUM covers a broader spectral range (100-1600 cm^{-1}) than IRIS-D, the DoFs for the atmospheric profiles and surface properties using FORUM measurements can be even higher. It has been shown by Ben-Yami et al. (2022) that DoFs for simulated FORUM measurements can be as high as 5 for the humidity profile and greater than 65 for far-IR surface emissivity when the precipitable water vapor is lower than 1mm.

Acknowledgement

We wish to thank two anonymous reviewers for their thoughtful comments and suggestions. We would like to pay our sincere tribute to R.A. Hanel and the whole IRIS-D instrument team for making such pioneering far-infrared satellite measurements half a century ago. We are thankful to X. Liu at NASA Langley for providing the PCRTM code to us. This research was carried out at the University of Michigan, Ann Arbor, and supported by the NASA PREFIRE mission under grant 80NSSC18K1485 with a subcontract from the University of Wisconsin. Portions of this research were carried out at the Jet Propulsion Laboratory, California Institute of Technology, under contract with the National Aeronautics and Space Administration.

Data availability statement

The data and software used in this study for analysis of synoptic patterns, information content, and retrieval estimates (Xie et al., 2022b) are available at Zenodo via https://doi.org/10.5281/zenodo.7300339. The IRIS-D level 1 radiance data v001, short name IRISN4RAD (Hanel et al., 1971; Hanel et al., 1972), are from the NASA Goddard Earth Sciences Data and Information Services Center (GES DISC) archive and can be obtained via the https://disc.gsfc.nasa.gov/datacollection/IRISN4RAD_001.html. The ECMWF ERA5 hourly reanalysis data of air temperature, specific humidity, and geopotential height on pressure levels (Hersbach et al., 2018a), as well as surface skin temperature, surface pressure and wind velocity on single levels (Hersbach et al., 2018b) used in this study were downloaded from the Copernicus Climate Change Service (C3S) Climate Data Store via https://cds.climate.copernicus.eu/cdsapp#!/search?text=ERA5%20hourly&type=dataset. The atmospheric CO_2 concentration data used in the study were obtained from the NOAA Global

Monitoring Laboratory (Tans & Keeling, 2022) through the webpage https://gml.noaa.gov/ccgg/trends/. The global surface spectral emissivity dataset (Huang et al., 2016) can be downloaded from https://huang.engin.umich.edu/data-products/.

Reference

Ackerman, S. A., Smith, W. L., Revercomb, H. E., & Spinhirne, J. D. (1990). The 27–28 October 1986 FIRE IFO Cirrus Case Study: Spectral Properties of Cirrus Clouds in the 8–12 μm Window, *Monthly Weather Review*, *118*(11), 2377-2388. https://doi.org/10.1175/1520-0493(1990)118<2377:TOFICC>2.0.CO;2

Backus, G., Gilbert, F., & Bullard, E. C. (1970). Uniqueness in the inversion of inaccurate gross Earth data. *Philosophical Transactions of the Royal Society of London. Series A, Mathematical and Physical Sciences, 266*(1173), 123-192. https://doi.org/10.1098/rsta.1970.0005

Bantges, R. J., Brindley, H. E., Chen, X. H., Huang, X. L., Harries, J. E., & Murray, J. E. (2016). On the Detection of Robust Multidecadal Changes in Earth's Outgoing Longwave Radiation Spectrum. *Journal of Climate, 29*(13), 4939-4947. https://doi.org/10.1175/jcli-d-15-0713.1

Becker, F., & Li, Z.-L. (1990). Towards a local split window method over land surfaces. *International Journal of Remote Sensing, 11*(3), 369-393. https://doi.org/10.1080/01431169008955028

Bell, B., Hersbach, H., Simmons, A., Berrisford, P., Dahlgren, P., Horányi, A., et al. (2021). The ERA5 global reanalysis: Preliminary extension to 1950. *Q J R Meteorol Soc*, 147(741), 4186– 4227. Available from: https://doi.org/10.1002/qj.4174

Bellisario, C., Brindley, H. E., Murray, J. E., Last, A., Pickering, J., Harlow, R. C., et al. (2017). Retrievals of the Far Infrared Surface Emissivity Over the Greenland Plateau Using the Tropospheric Airborne Fourier Transform Spectrometer (TAFTS). *Journal of Geophysical Research: Atmospheres, 122*(22), 12,152-112,166. https://doi.org/10.1002/2017JD027328

Ben-Yami, M., Oetjen, H., Brindley, H., Cossich, W., Lajas, D., Maestri, T., Magurno, D., Raspollini, P., Sgheri, L., and Warwick, L. (2022) Emissivity retrievals with FORUM's end-to-end simulator: challenges and recommendations, *Atmos. Meas. Tech.*, 15, 1755–1777. https://doi.org/10.5194/amt-15-1755-2022

Borel, C. C. (1998). Surface emissivity and temperature retrieval for a hyperspectral sensor. *IEEE International Geoscience and Remote Sensing. Symposium Proceedings, 1,* 546-549. https://doi.org/10.1109/IGARSS.1998.702966.

Carissimo, A., De Feis, I., & Serio, C. (2005). The physical retrieval methodology for IASI: the δ-IASI code. *Environmental Modelling & Software, 20*(9), 1111-1126. https://doi.org/10.1016/j.envsoft.2004.07.003

Chen, X., Huang, X., Dong, X., Xi, B., Dolinar, E. K., Loeb, N. G., et al. (2018). Using AIRS and ARM SGP Clear-Sky Observations to Evaluate Meteorological Reanalyses: A Hyperspectral Radiance Closure Approach. *Journal of Geophysical Research: Atmospheres, 123*(20), 11,720-711,734. https://doi.org/10.1029/2018JD028850

Chen, X., Huang, X., & Flanner, M. G. (2014). Sensitivity of modeled far-IR radiation budgets in polar continents to treatments of snow surface and ice cloud radiative properties. *Geophysical Research Letters, 41*(18), 6530-6537. https://doi.org/10.1002/2014GL061216

Chen, X., Huang, X., & Liu, X. (2013). Non-negligible effects of cloud vertical overlapping assumptions on

longwave spectral fingerprinting studies. *Journal of Geophysical Research: Atmospheres, 118*(13), 7309-7320. https://doi.org/10.1002/jgrd.50562

Clough, S. A., Shephard, M. W., Mlawer, E. J., Delamere, J. S., Iacono, M. J., Cady-Pereira, K., et al. (2005). Atmospheric radiative transfer modeling: a summary of the AER codes. *Journal of Quantitative Spectroscopy and Radiative Transfer, 91*(2), 233-244. https://doi.org/10.1016/j.jqsrt.2004.05.058

Davis, S. M., Hegglin, M. I., Fujiwara, M., Dragani, R., Harada, Y., Kobayashi, C., Long, C., Manney, G. L., Nash, E. R., Potter, G. L., Tegtmeier, S., Wang, T., Wargan, K., and Wright, J. S. (2017). Assessment of upper tropospheric and stratospheric water vapor and ozone in reanalyses as part of S-RIP, *Atmospheric Chemistry and Physics*, *17*, 12743–12778. https://doi.org/10.5194/acp-17-12743-2017

Faysash, D. A., & Smith, E. A. (2000). Simultaneous Retrieval of Diurnal to Seasonal Surface Temperatures and Emissivities over SGP ARM–CART Site Using GOES Split Window, *Journal of Applied Meteorology*, *39*(7), 971-982. https://doi.org/10.1175/1520-0450(2000)039<0971:SRODTS>2.0.CO;2

Feldman, D. R., Collins, W. D., Pincus, R., Huang, X., & Chen, X. (2014). Far-infrared surface emissivity and climate. *Proceedings of the National Academy of Sciences, 111*(46), 16297. https://doi.org/10.1073/pnas.1413640111

Gillespie, A., Rokugawa, S., Matsunaga, T., Cothern, J. S., Hook, S., & Kahle, A. B. (1998). A temperature and emissivity separation algorithm for Advanced Spaceborne Thermal Emission and Reflection Radiometer (ASTER) images. *IEEE Transactions on Geoscience and Remote Sensing, 36*(4), 1113-1126. https://doi.org/10.1109/36.700995.

Hanel, R. A., Conrath, B. J., Kunde, V. G., Prabhakara, C., Revah, I., Salomonson, V. V. and Wolford, G. (1972). The Nimbus 4 infrared spectroscopy experiment: 1. Calibrated thermal emission spectra, *J. Geophys. Res.*, 77(15), 2629– 2641, https://doi.org/10.1029/JC077i015p02629.

Hanel, R. A., Schlachman, B., Rogers, D., & Vanous, D. (1971). Nimbus 4 Michelson Interferometer. *Applied Optics, 10*(6), 1376-1382. https://doi.org/10.1364/AO.10.001376

Harries, J., Brindley, H., Sagoo, P., & Bantges, R. (2001). Increases in greenhouse forcing inferred from the outgoing longwave radiation spectra of the Earth in 1970 and 1997. *Nature 410*, 355–357. https://doi.org/10.1038/35066553

Haskins, R. D., Goody, R. M., and Chen, L. (1997), A statistical method for testing a general circulation model with spectrally resolved satellite data, *J. Geophys. Res.*, 102(D14), 16563–16581. https://doi.org/10.1029/97JD00897

Haskins, R., Goody, R., & Chen, L. (1999). Radiance Covariance and Climate Models, *Journal of Climate*, *12*(5), 1409-1422. https://doi.org/10.1175/1520-0442(1999)012<1409:RCACM>2.0.CO;2

Hersbach, H., Bell, B., Berrisford, P., Hirahara, S., Horányi, A., Muñoz-Sabater, J., et al. (2020). The ERA5 global reanalysis. *Quarterly Journal of the Royal Meteorological Society, 146*(730), 1999-2049. https://doi.org/10.1002/qj.3803

Hersbach, H., Bell, B., Berrisford, P., Biavati, G., Horányi, A., Muñoz Sabater, J., Nicolas, J., Peubey, C., Radu, R., Rozum, I., Schepers, D., Simmons, A., Soci, C., Dee, D., Thépaut, J-N. (2018a): ERA5 hourly data on pressure levels from 1959 to present. [Dataset] Copernicus Climate Change Service (C3S) Climate Data Store (CDS). https://doi.org/10.24381/cds.bd0915c6

Hersbach, H., Bell, B., Berrisford, P., Biavati, G., Horányi, A., Muñoz Sabater, J., Nicolas, J., Peubey, C., Radu, R., Rozum, I., Schepers, D., Simmons, A., Soci, C., Dee, D., Thépaut, J-N. (2018b): ERA5 hourly data on single levels from 1959 to present. [Dataset] Copernicus Climate Change Service (C3S) Climate Data Store (CDS). https://doi.org/10.24381/cds.adbb2d47

Huang, X., Chen, X., Flanner, M., Yang, P., Feldman, D., & Kuo, C. (2018). Improved Representation of

Surface Spectral Emissivity in a Global Climate Model and Its Impact on Simulated Climate. *Journal of Climate, 31*(9), 3711-3727. https://doi.org/10.1175/jcli-d-17-0125.1

Huang, X., Chen, X., Soden, B. J., & Liu, X. (2014). The spectral dimension of longwave feedback in the CMIP3 and CMIP5 experiments. *Geophysical Research Letters, 41*(22), 7830-7837. https://doi.org/10.1002/2014GL061938

Huang, X., Chen, X., Zhou, D. K., & Liu, X. (2016). An Observationally Based Global Band-by-Band Surface Emissivity Dataset for Climate and Weather Simulations. *Journal of the Atmospheric Sciences, 73*(9), 3541-3555. https://doi.org/10.1175/jas-d-15-0355.1

Huang, X., Farrara, J., Leroy, S. S., Yung, Y. L., and Goody, R. M. (2002). Cloud variability as revealed in outgoing infrared spectra: Comparing model to observation with spectral EOF analysis, *Geophys. Res. Lett.*, 29(8). https://doi.org/10.1029/2001GL014176

Huang, X., Ramaswamy, V., and Schwarzkopf, M. D. (2006). Quantification of the source of errors in AM2 simulated tropical clear-sky outgoing longwave radiation, *J. Geophys. Res.*, 111, D14107. https://doi.org/10.1029/2005JD006576

L'Ecuyer, T. S., Drouin, B. J., Anheuser, J., Grames, M., Henderson, D., Huang, X., et al. (2021). The Polar Radiant Energy in the Far InfraRed Experiment: A New Perspective on Polar Longwave Energy Exchanges. *Bulletin of the American Meteorological Society*, 1-46. https://doi.org/10.1175/BAMS-D-20-0155.1

L'Ecuyer, T. S., & Stephens, G. L. (2002). An Estimation-Based Precipitation Retrieval Algorithm for Attenuating Radars. *Journal of Applied Meteorology*, 41(3), 272-285. https://doi.org/10.1175/1520-0450(2002)041<0272:AEBPRA>2.0.CO;2

Li, J., Li, J., Weisz, E., and Zhou, D. K. (2007), Physical retrieval of surface emissivity spectrum from hyperspectral infrared radiances, *Geophys. Res. Lett.*, 34, L16812, https://doi.org/10.1029/2007GL030543

Li, J., Wolf, W. W., Menzel, W. P., Zhang, W., Huang, H., & Achtor, T. H. (2000). Global Soundings of the Atmosphere from ATOVS Measurements: The Algorithm and Validation, *Journal of Applied Meteorology*, *39*(8), 1248-1268. https://doi.org/10.1175/1520-0450(2000)039<1248:GSOTAF>2.0.CO;2

Liu, X., Smith, W. L., Zhou, D. K., & Larar, A. (2006). Principal component-based radiative transfer model for hyperspectral sensors: theoretical concept. *Applied Optics, 45*(1), 201-209. https://doi.org/10.1364/AO.45.000201

Liu, X., Zhou, D. K., Larar, A. M., Smith, W. L., Schluessel, P., Newman, S. M., et al. (2009). Retrieval of atmospheric profiles and cloud properties from IASI spectra using super-channels. *Atmos. Chem. Phys., 9*(23), 9121-9142. https://doi.org/10.5194/acp-9-9121-2009

Ma, X., Wan, Z., Moeller, C., Menzel, W., Gumley, L., and Zhang, Y. (2000). Retrieval of geophysical parameters from Moderate Resolution Imaging Spectroradiometer thermal infrared data: evaluation of a two-step physical algorithm, *Appl. Opt.* 39, 3537-3550. https://doi.org/10.1364/AO.41.000909

Maahn, M., Turner, D. D., Löhnert, U., Posselt, D. J., Ebell, K., Mace, G. G., & Comstock, J. M. (2020). Optimal Estimation Retrievals and Their Uncertainties: What Every Atmospheric Scientist Should Know. *Bulletin of the American Meteorological Society, 101*(9), E1512-E1523. https://doi.org/10.1175/bams-d-19-0027.1

Masiello, G., Serio, C., Venafra, S., Liuzzi, G., Poutier, L., Göttsche, F-M. (2018). Physical Retrieval of Land Surface Emissivity Spectra from Hyper-Spectral Infrared Observations and Validation with In Situ Measurements. *Remote Sensing*, *10*(6):976. https://doi.org/10.3390/rs10060976

Murray, J. E., Brindley, H. E., Fox, S., Bellisario, C., Pickering, J. C., Fox, C., et al. (2020). Retrievals of High-Latitude Surface Emissivity Across the Infrared From High-Altitude Aircraft Flights. *Journal of Geophysical Research: Atmospheres, 125*(22), e2020JD033672. https://doi.org/10.1029/2020JD033672

Palchetti, L., Brindley, H., Bantges, R., Buehler, S. A., Camy-Peyret, C., Carli, B., et al. (2020). FORUM: Unique Far-Infrared Satellite Observations to Better Understand How Earth Radiates Energy to Space. *Bulletin of the American Meteorological Society, 101*(12), E2030-E2046. https://doi.org/10.1175/bams-d-19-0322.1

Plokhenko, Y., & Menzel, W. P. (2000). The Effects of Surface Reflection on Estimating the Vertical Temperature–Humidity Distribution from Spectral Infrared Measurements, *Journal of Applied Meteorology*, *39*(1), 3-14. https://doi.org/10.1175/1520-0450(2000)039<0003:TEOSRO>2.0.CO;2

Rodgers, C. D. (2000). *Inverse Methods for Atmospheric Sounding: Theory and Practice* (Vol. 2 256 pp): WORLD SCIENTIFIC, ISBN: 978-981-02-2740-1.

Ridolfi, M., Del Bianco, S., Di Roma, A., Castelli, E., Belotti, C., Dandini, P., Di Natale, G., Dinelli, BM., C.-Labonnote, L., Palchetti, L. (2020). FORUM Earth Explorer 9: Characteristics of Level 2 Products and Synergies with IASI-NG, *Remote Sensing*.12(9), 1496. https://doi.org/10.3390/rs12091496

Scarlat, R. C., Heygster, G., & Pedersen, L. T. (2017). Experiences With an Optimal Estimation Algorithm for Surface and Atmospheric Parameter Retrieval from Passive Microwave Data in the Arctic. *IEEE Journal of Selected Topics in Applied Earth Observations and Remote Sensing, 10*(9), 3934-3947. https://doi.org/10.1109/JSTARS.2017.2739858

Sgheri, L., Belotti, C., Ben-Yami, M., Bianchini, G., Carnicero Dominguez, B., Cortesi, U., Cossich, W., Del Bianco, S., Di Natale, G., Guardabrazo, T., Lajas, D., Maestri, T., Magurno, D., Oetjen, H., Raspollini, P., and Sgattoni, C. (2022). The FORUM end-to-end simulator project: architecture and results, *Atmos. Meas. Tech.*, 15, 573–604. https://doi.org/10.5194/amt-15-573-2022

Susskind, J., Barnet, C. D. and Blaisdell, J. M. (2003). Retrieval of atmospheric and surface parameters from AIRS/AMSU/HSB data in the presence of clouds, *IEEE Transactions on Geoscience and Remote Sensing*, 41(2), 390-409. https://doi.org/10.1109/TGRS.2002.808236.

Tans, P. and Keeling, R. (2022). Atmospheric Carbon Dioxide Dry Air Mole Fractions from quasi-continuous measurements at Mauna Loa, Hawaii, 1971-2021, Version 2022-05 [Dataset]. National Oceanic and Atmospheric Administration (NOAA) / Global Monitoring Laboratory (GML) (http://gml.noaa.gov/ccgg/trends/) and Scripps Institution of Oceanography (http://scrippsco2.ucsd.edu/). https://doi.org/10.15138/yaf1-bk21

Turner, D. D., & Löhnert, U. (2014). Information Content and Uncertainties in Thermodynamic Profiles and Liquid Cloud Properties Retrieved from the Ground-Based Atmospheric Emitted Radiance Interferometer (AERI). *Journal of Applied Meteorology and Climatology, 53*(3), 752-771. https://doi.org/10.1175/jamc-d-13-0126.1

Wan, Z. (2008). New refinements and validation of the MODIS Land-Surface Temperature/Emissivity products. *Remote Sensing of Environment*, *112*(1), 59-74. https://doi.org/10.1016/j.rse.2006.06.026.

Wood, N. B., & L'Ecuyer, T. S. (2021). What millimeter-wavelength radar reflectivity reveals about snowfall: an information-centric analysis. *Atmos. Meas. Tech., 14*(2), 869-888. https://doi.org/10.5194/amt-14-869-2021.

Xie, Y., Huang, X., Chen, X., L'Ecuyer, T. S., Drouin, B. J., & Wang, J. (2022a). Retrieval of surface spectral emissivity in polar regions based on the optimal estimation method. *Journal of Geophysical Research: Atmospheres*, 127, e2021JD035677. https://doi.org/10.1029/2021JD035677

Xie, Y., Huang, X., Chen, X., L'Ecuyer, T. S., & Drouin, B. J. (2022b). Joint Use of Far-Infrared and Mid-

Infrared Observation for Sounding Retrievals: Learning from the Past for Upcoming Far-Infrared Missions Version 1 [Dataset]. Zenodo. https://doi.org/10.5281/zenodo.7300339

Zhou, D. K., Larar, A. M., Liu, X., Smith, W. L., Strow, L. L., Yang, P., et al. (2011). Global Land Surface Emissivity Retrieved From Satellite Ultraspectral IR Measurements. *IEEE Transactions on Geoscience and Remote Sensing, 49*(4), 1277-1290. https://doi.org/10.1109/TGRS.2010.2051036

Zhou, D. K., Smith, W. L., Liu, X., Larar, A. M., Mango, S. A., & Huang, H.-L. (2007). Physically Retrieving Cloud and Thermodynamic Parameters from Ultraspectral IR Measurements. *Journal of the Atmospheric Sciences, 64*(3), 969-982. https://doi.org/10.1175/jas3877.1

Table 1. Basic information of the selected cases

Case NO.	Geolocation	Time	Surface Pressure
1	(80.0ºN, 43.4ºE)	April 21 3:25 am UTC, 1970	1027.2hPa
2	(76.2ºN, 215.4ºE)	July 13 6:29 pm UTC, 1970	1015.1hPa

Table 2. Degree of Freedom for signals of the state variables.

	Specific humidity (log)	Temperature	Surface skin temperature	Surface spectral emissivity (logit)	
				mid-IR	far-IR
Case 1	1.32	4.13	0.99	24.92	10.60
Case 2	1.91	4.03	0.97	24.21	0.01

Table 3. Average relative uncertainty of state variables before and after the retrieval. The *a priori* relative uncertainty is calculated as the ratio of *a priori* uncertainty to the *a priori* mean. The *posteriori* relative uncertainty is calculated as the ratio of retrieval uncertainty to the retrieved state variables.

Average relative uncertainty (%)		Specific humidity (log)	Temperature	Surface skin temperature	Surface spectral emissivity (logit)	
					mid-IR	far-IR
Case 1	*a priori*	179.4	3.4	4.6	31.1	18.3
	posteriori	25.7	2.4	0.1	16.7	8.5
Case 2	*a priori*	98.3	1.7	2.4	31.1	18.3
	posteriori	58.3	1.2	0.1	28.8	9.4

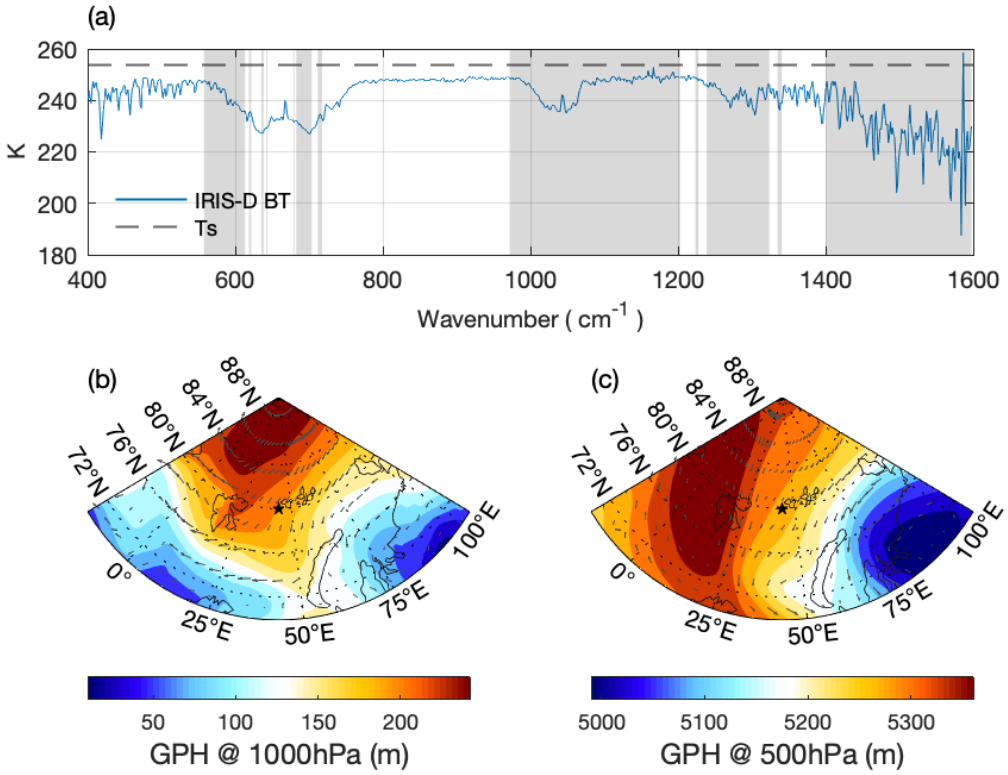

Figure 1. (a) The IRIS-D spectra of Case 1 shown in brightness temperature. It was measured on April 21, 1970 at 80.0ºN, 43.4ºE. The dashed line denotes the corresponding surface skin temperature from the ERA5 hourly reanalysis data. The gray shades denote the IRIS-D channels not used in the retrieval due to (1) absorption of greenhouse gases other than H_2O and CO_2, i.e., O_3, CO, N_2O and CH_4, and (2) large measurement noises (1400-1600 cm^{-1}). (b) ERA5 1000-hPa geopotential height (GPH) in color and the horizontal wind field for the time of observation. The black pentagram marks the geolocation of Case 1. (c) Same as (b) but on 500hPa pressure level.

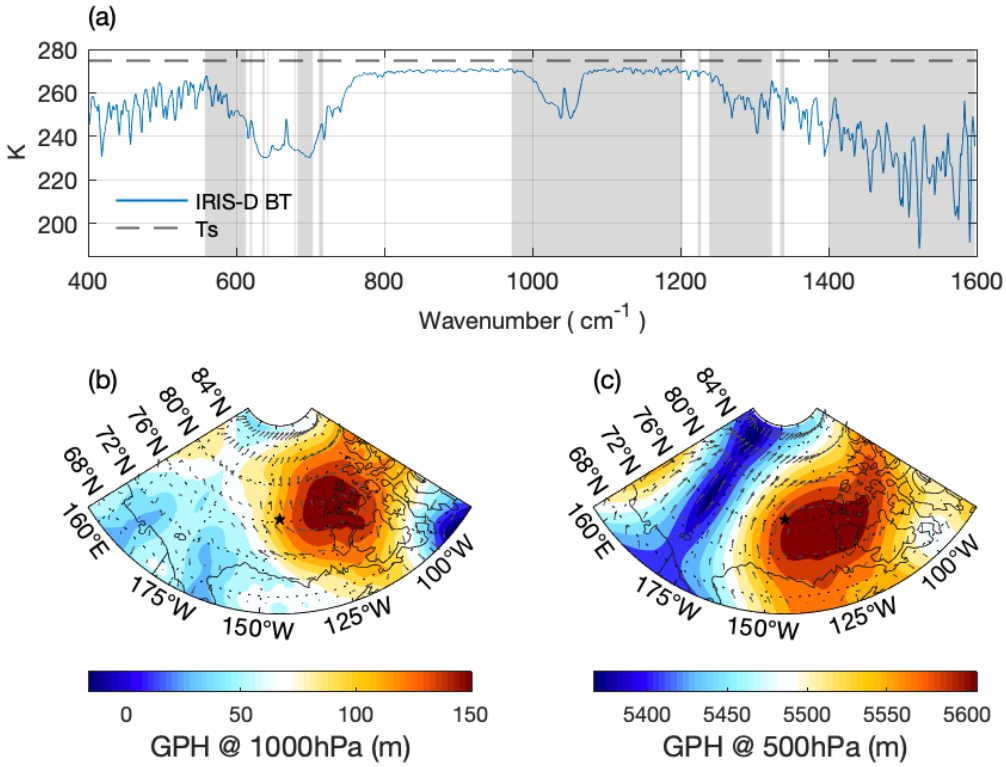

Figure 2. Same as Figure 1, but for the Case 2 observed on July 13, 1970 at 76.2ºN, 215.4ºE.

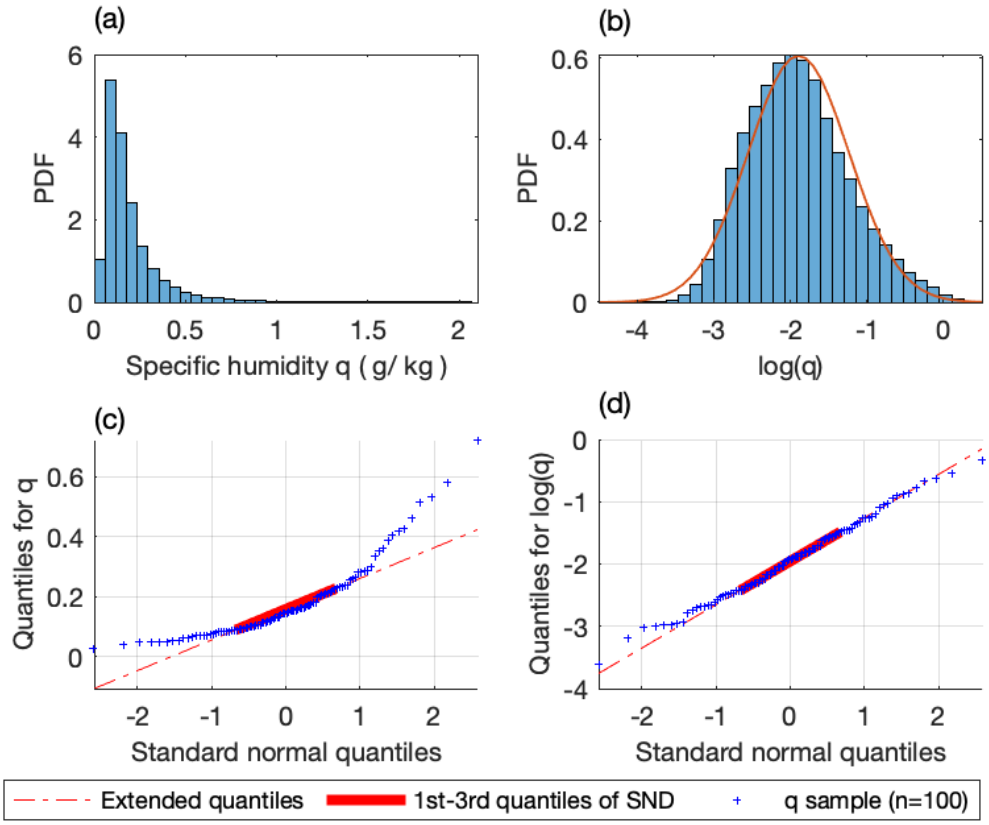

Figure 3. (a) Probability density function (PDF) of the Arctic 500-hPa specific humidity based on the ERA5 hourly reanalysis data in March, April, and May 1970. (b) PDF of the logarithmic transformation of the specific humidity in (a). The red curve represents the theoretical PDF of a Gaussian distribution with identical mean and standard deviation. (c) Quantiles of the specific humidity samples from (a) (sample size = 100) versus the theoretical quantiles of the standard normal distribution (SND). (d) Same as (c), but for the logarithmically transformed specific humidity at 500hPa.

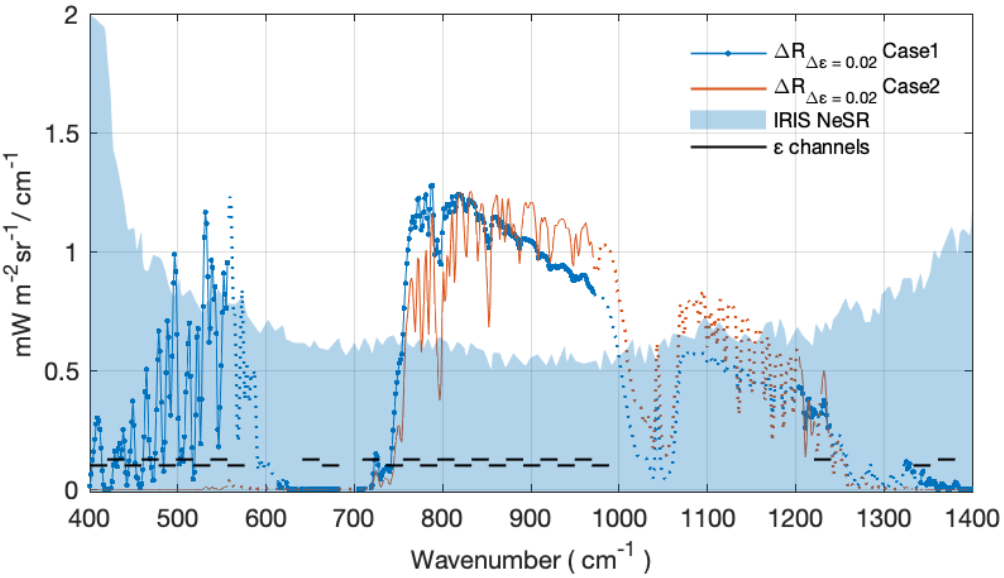

Figure 4. Radiances change at TOA in response to an increase of surface spectral emissivity by 0.02 for Case 1 and Case 2, denoted by blue curve with dot and red curve, respectively. For both curves, solid part represents the selected IRIS-D channels used in the retrieval, while the dotted part represents the channels not used in the retrievals (refers to Section 2.1 for further details.) The blue shade denotes the IRIS-D NeSR (1σ). The black horizontal lines, each covering a 10 cm^{-1} spectral interval, indicate channels on which surface spectral emissivity are retrieved.

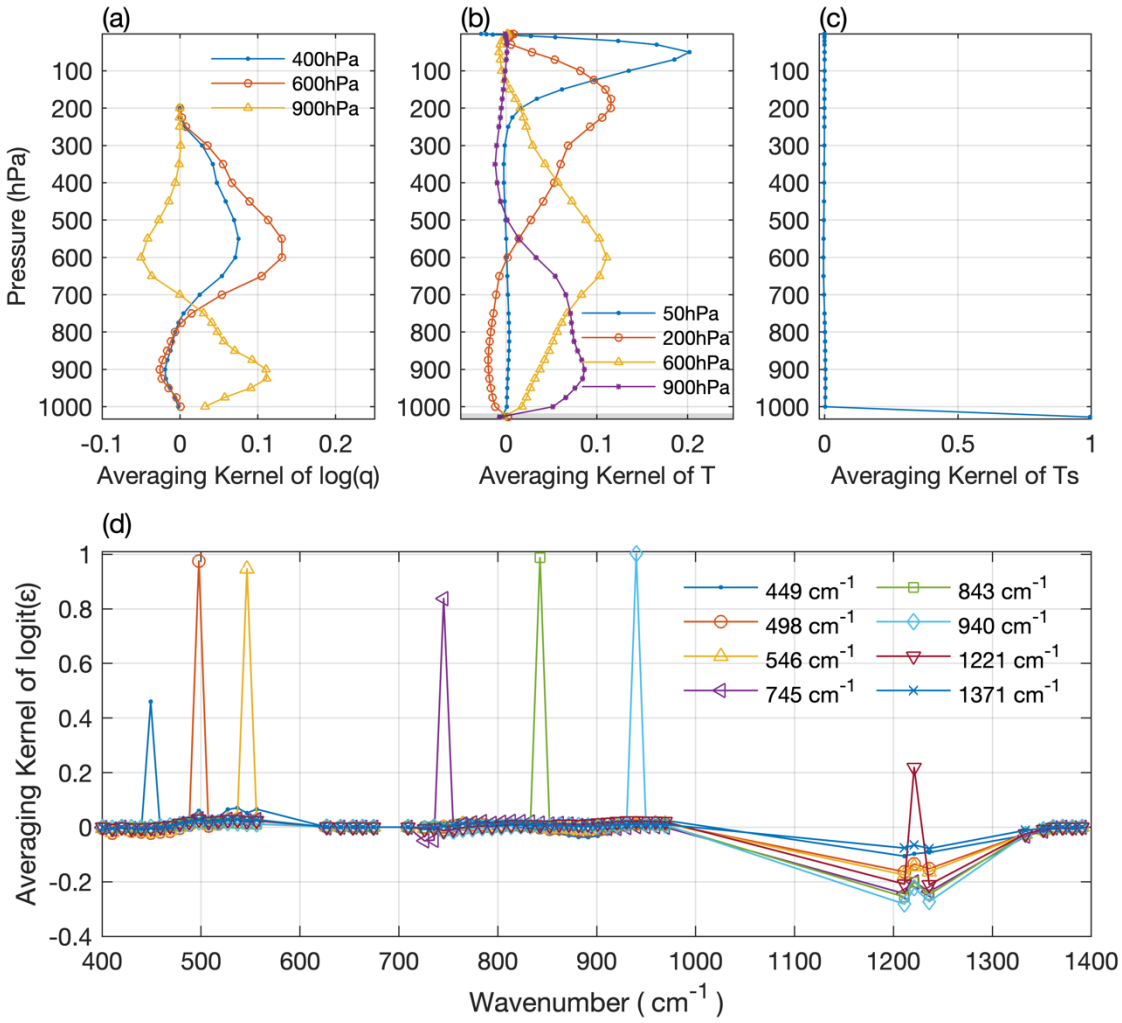

Figure 5. Averaging kernels of selected state variables in Case 1: (a) for logarithmic specific humidity on pressure levels of 400hPa, 600hPa and 900hPa, (b) for air temperature on four pressure levels from middle stratosphere to lower troposphere (c) for surface skin temperature, and (d) for logit-transformed surface spectral emissivity on eight random channels. The shaded layer in subpanel (b) is to highlight the pressure level of surface skin temperature. For better visualization, the averaging kernels for humidity and temperature at other pressure levels are not shown.

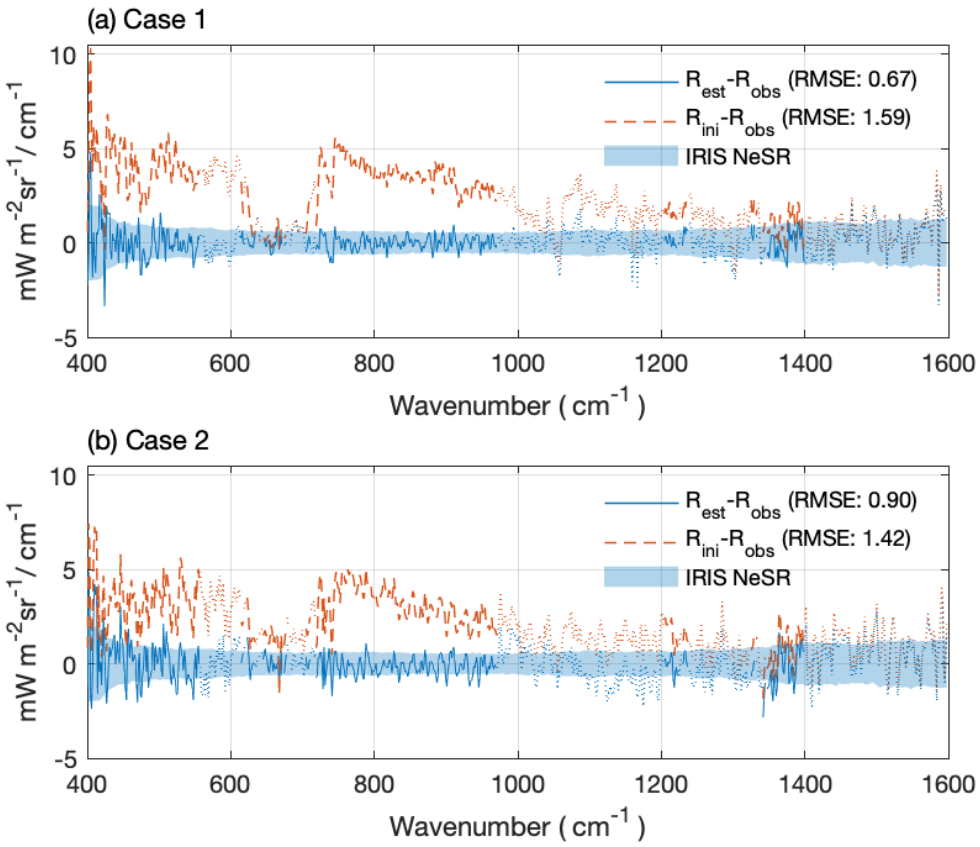

Figure 6. (a) The blue curve represents the difference between the radiances based on the retrieved state variables and the IRIS-D observations, i.e., the residual radiances for Case 1 on April 21, 1970, and the root-mean-squared error (RMSE) is 0.67 $\mathrm{mW \cdot m^{-2} sr^{-1} / cm^{-1}}$. The red dash curve represents the residual radiances based on the initial guess which consists of the temperature and humidity fields from the ERA5 hourly reanalysis and constant surface spectral emissivity at 0.95. Its RMSE is 1.59 $\mathrm{mW \cdot m^{-2} sr^{-1} / cm^{-1}}$. As in previous figures, solid part denotes the selected channels used in the retrieval while the dotted part denotes the channels not used in the retrieval. The blue shade represents the IRIS-D NeSR ($\pm 1\sigma$). (b) Same as (a), but for the Case 2 measured on July 13, 1970.

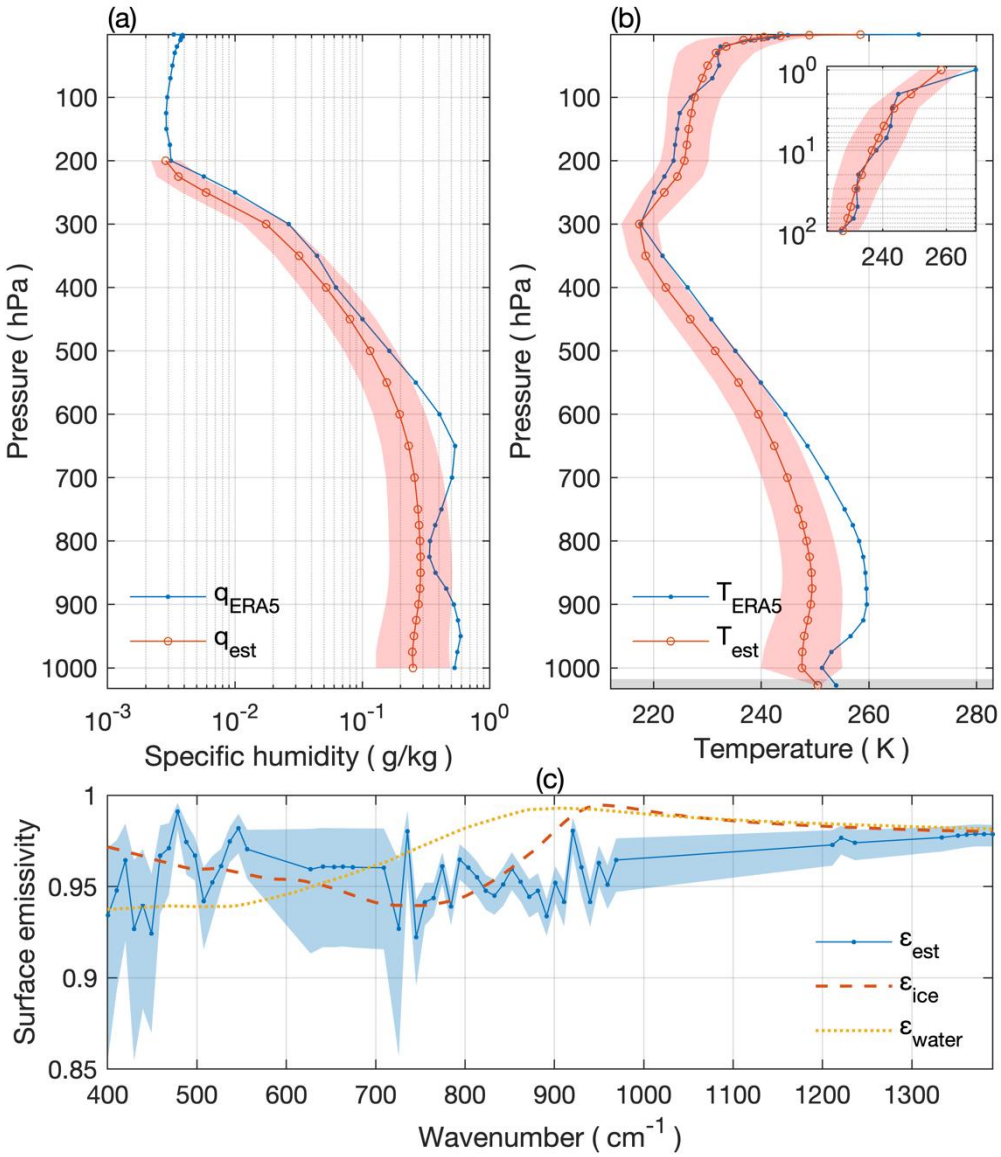

Figure 7. Retrieval estimates of the state variables for Case 1 on April 21, 1970. (a) The blue curve represents the specific humidity profile from the ERA5 hourly reanalysis up to 1hPa (i.e., initial guess). The red curve represents the retrieved specific humidity between 200-1000hPa with the retrieval uncertainty denoted by the red shade. (b) Similar to (a), but for the temperature profile from 1hPa to the surface. The shaded layer is to highlight the pressure level of surface skin temperature. (c) The blue curve represents the retrieved surface spectral emissivity with the retrieval uncertainty denoted by the blue shade. The surface emissivity spectra for ice and water are from a global surface emissivity database (Huang et al., 2016).

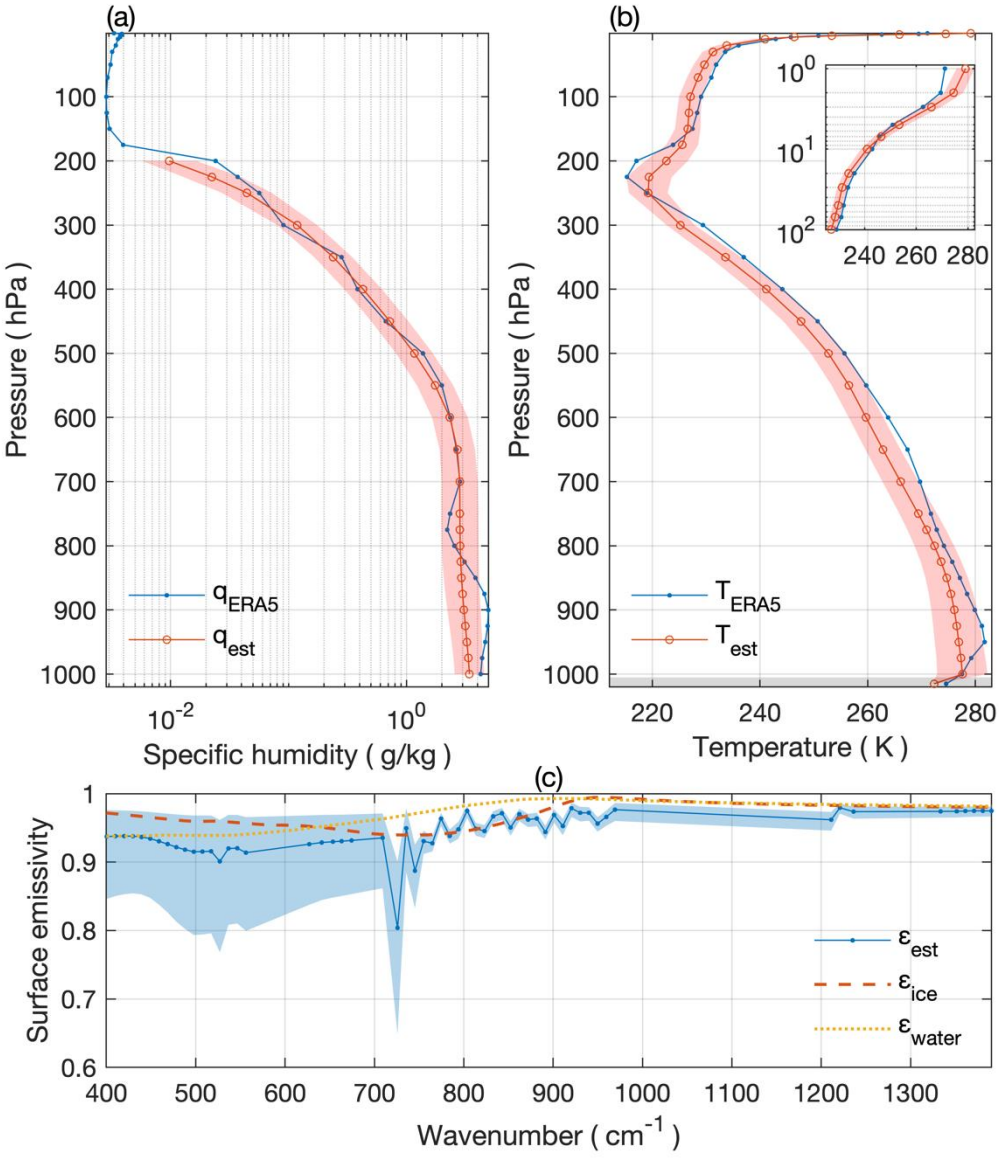

Figure 8. Same as Figure 7, but for the Case 2 observed on July 13, 1970.

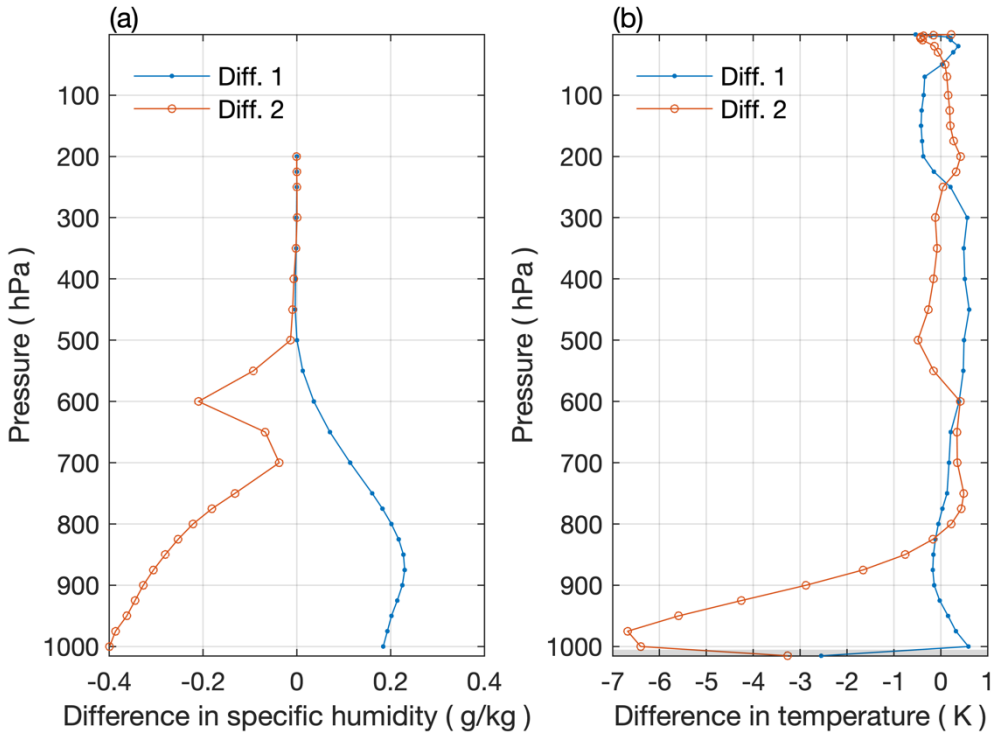

Figure 9. Differences in the retrieved atmospheric humidity (a) and temperature profiles (b) between two configurations: (1) blackbody assumption for surface emissivity and (2) simultaneous retrieval of surface spectral emissivity together with other state variables. Blue lines with filled dots (Diff. 1) denote differences between two configurations for Case 1. Red lines with open circles (Diff. 2) represent differences between two configurations for Case 2. Shaded layer in subpanel (b) highlights the pressure level of surface skin temperature.